PAPER

Design of a 3-D Printed, Modular Lateral Line Sensory System for Hydrodynamic Force Estimation

AUTHORS
Kevin Nelson
Department of Electrical and
Computer Engineering, University
of Florida

Kamran Mohseni
Department of Electrical and
Computer Engineering, Department
of Mechanical and Aerospace
Engineering, and Institute for
Networked Autonomous Systems,
University of Florida

ABSTRACT

This paper presents a sensory system that is biologically inspired by the lateral line sensory system found in fish. This artificial lateral line system provides sensory information to be used in vehicle control algorithms, both to reduce model complexity and to measure hydrodynamic disturbances. The system presented in this paper is a modular implementation that can fit around a vehicle without requiring modifications to the hull. The design and manufacturing processes are presented in detail along with considerations for sensor placement and port spacing. An algorithm for calculating the hydrodynamic forces acting on the surface of a vehicle is derived and experimentally validated. An underwater motion capture system and strain sensors are used to calculate a reference hydrodynamic force that compares favorably with the hydrodynamic force calculated by the lateral line system.

Keywords: AUV, bio-inspired, lateral line, sensory system

Introduction

Many researchers believe that the lateral line, a sensory system found in most fish and other aquatic organisms (Blaxter, 1987), plays an integral role in many behaviors such as rheotaxis (Montgomery et al., 1997), schooling (Pitcher et al., 1976; Coombs, 2001), detection of obstacles and other organisms (Bleckmann, 2008), predation (Montgomery & Macdonald, 1987; Coombs et al., 2001; Pohlmann et al., 2004), and communication (Satou et al., 1994). The lateral line contains distributed sensory organs called neuromasts. Most lateral lines contain two distinct types of neuromasts: superficial neuromasts and canal neuromasts. Experiments suggest that superficial neuromasts are sensitive to lower-frequency signals, whereas canal neuromasts respond to higher-frequency signals (Kroese & Schellart, 1992). The superficial neuromasts are believed to measure the relative flow velocity over the skin of the fish (Kroese et al., 1978; Coombs & Montgomery, 1994; Montgomery et al., 2000). The canal neuromasts provide complementary information, measuring the acceleration of the fluid (Muñz, 1989).

Inspired by the role the lateral line plays in aquatic organisms, many researchers have attempted to replicate the sensing capabilities of this system by designing and fabricating custom sensors. For example, researchers have attempted to use micromachined flow sensors mimicking cilium to measure flow rate (Fan et al., 2002). In McConney et al. (2009), an artificial cupula mimicking the superficial neuromast was manufactured to have reasonable sensitivity. An array of micromachined artificial hair cell sensors was used to attempt to detect and localize a dipole flow source (Dagamesh et al., 2013). In Abdulsadda and Tan (2013), it is shown that dipole detection and localization can also be performed using ionic polymer-metal composite (IPMC) sensors. Researchers have used microelectromechanical systems (MEMS) pressure sensors manufactured with a liquid crystal polymer (LCP) membrane in attempts to sense flow rate and direction (Kottapalli et al., 2011). An array of these sensors was later used to try to detect background flow velocity and the velocity of passing object (Kottapalli et al., 2012). MEMS sensors inspired by superficial neuromasts were suggested to be capable of detecting flow velocities; when these sensors were embedded in polydimethylsiloxane (PDMS), canal experiments suggest that the static component of the flow was filtered out (Kottapalli et al., 2014); however, it also appears to reduce the sensitivity of the sensors. Additionally, researchers have used optical flow sensors mimicking canal neuromasts to detect flow properties (Klein & Bleckmann, 2011). While they have reasonable results, the primary disadvantage of using custom-made sensors is added complexity; these sensors add difficulty to the manufacturing process and require additional calibration and testing to ensure every sensor is working. Additionally, sensors mimicking superficial neuromasts generally have a delicate sensing element that is susceptible to being damaged.

Due to the complexity and cost of manufacturing custom sensors, many other researchers have used off-the-shelf sensors to validate the functionalities of the lateral line. In Fernandez et al. (2011), a linear array of pressure sensors was used to determine the position, shape, and size of various objects in a flow. Chambers et al. (2014) attempted to use absolute pressure sensors to detect the turbulent wake of a cylinder; these sensors suffered from low resolution, requiring amplification and high-precision analog-to-digital converters (ADCs) to achieve moderate sensor resolution. Akanyeti et al. (2013) suggested that an artificial lateral line system can be used to monitor the speed and acceleration of a marine craft; however, the error of the method tends to scale with velocity suggesting that it is not suitable for fast-moving vehicles. In another work, a lateral line system implementing pressure sensors was used to try to detect the angle of attack of a marine craft for use in active yaw control; the system was able to achieve reasonable results after advanced filtering techniques were applied (Gao & Triantafyllou, 2012). Researchers attempted to use a multimodal lateral line system using both custom hair cell sensors and off-the-shelf pressure sensors to aid in rheotaxis and station holding (Devries et al., 2015). Many of the aforementioned works used absolute and gauge pressure sensors. The primary disadvantage of these sensors is that they have a low sensitivity when compared to differential pressure sensors (such as those we use in this work), requiring amplifier circuitry and high-precision ADCs to achieve similar results to the differential sensors. This adds additional complexity to the system and requires additional computations to process the data.

This paper continues our study of the lateral line sensory system and its application to vehicle control. Previously, in Ren and Mohseni (2012), we developed an airfoil model of a fish in a vortex street and showed that a lateral line is capable of sensing various parameters associated with the vortex street, including the distance from the vortices, the vortex spacing, and the vortex strength. The vortex street can represent the wake produced by a bluff body (i.e., an obstacle) in a flow, or it can represent the wake of a fish or ship (Ren & Mohseni, 2012). In Xu and Mohseni (2017), we designed and built a lateral line system capable of estimating the hydrodynamic forces acting on a body and showed that, if such a system were implemented on a vehicle, it could greatly aid in control strategies (see Figures 3(a) and 3(b) for pictures of these systems). In Ren and Mohseni (2014), we developed a model for the detection of a wall using a lateral line sensory system. We validated the force estimation and wall detection algorithms using lateral line systems with statically placed sensors (Xu & Mohseni, 2017). These systems were specially designed for validation purposes and could not be directly implemented on our group's vehicle without major modification to its hull, leading us to design a modular lateral line system (as shown in Figure 3(c)). The current work presents a modular lateral line system designed to easily fit around any underwater vehicle. A force estimation algorithm is derived and experimentally validated. Sensor placement methods for differential sensors are also discussed.

This paper is organized as follows: first, we present the primary motivation for developing the lateral line system, followed by a brief discussion of our group's vehicle. Next, we discuss in detail the design and manufacturing process for the modular lateral line. Finally, we discuss a force estimation algorithm and present experimental validation of the said algorithm.

Application to Vehicle Control

Our primary motivation for developing an artificial lateral line sensory system is the various benefits it could provide for vehicle control. One such application is vehicle modeling. Traditionally, underwater vehicles are modeled by a set of coupled differential equations (Fossen, 2011) representing the governing dynamics of a 6 degree-of-freedom body, given by

$$\dot{\eta} = J_{\Theta}(\eta)v, \tag{1}$$

$$M\dot{v} + C(v)v + D(v)v + g(\eta) + g_0 = \tau_c + \tau_{wave} + \tau_{wind}, \tag{2}$$

where $\eta = [x, y, z, \alpha, \beta, \gamma]^T$ in which x, y, and z are positions in the global frame and α, β, and γ are the roll, pitch, and yaw Euler angles of the rigid body using the *zyx* convention. The vector $v \in \mathbb{R}^6$ contains the linear and angular velocity of the vehicle expressed in the body-fixed frame. The term $M \in \mathbb{R}^{6\times6}$ represents a matrix containing the inertial terms, $C(v) \in \mathbb{R}^{6\times6}$ is a matrix containing the Coriolis/centrifugal terms, and $D(v) \in \mathbb{R}^{6\times6}$ represents a matrix containing the drag terms. The vector $g(\eta) \in \mathbb{R}^6$ represents the restoring forces acting on the vehicle. The vector $\tau_c = [F_x, F_y, F_z, \tau_\alpha, \tau_\beta, \tau_\gamma]^T$ denotes the control forces and moments. τ_{wave} and $\tau_{\text{wind}} \in \mathbb{R}^6$ represent vectors of disturbance forces and moments due to waves and wind, respectively. Finally, $J_\Theta(\eta)$ represents the velocity transformation from the inertial frame to the body-fixed frame.

The inertial matrix and Coriolis/centrifugal matrix are both composed of elements that are the sum of the components of the rigid body plus terms from the added mass. These terms, along with the drag terms and restoring forces, are due to hydrodynamic forces acting on the vehicle. Generally, these coefficients are characterized by running the vehicle in nearly static background conditions, essentially linearizing the governing equations of the fluid acting on the vehicle. Usually, this characterization causes some uncertainty to creep into the vehicle model, especially as the state of the vehicle deviates from the trim conditions of the vehicle during the linearization process. By directly measuring the pressure distribution over the vehicle, these forces can be calculated along with the hydrodynamic disturbance forces (due to waves, currents, etc.). This greatly simplifies the model of the vehicle and reduces the uncertainties inherent in the modeling process, allowing for an improved controller performance.

In Xu and Mohseni (2014), we present the dynamic equation of the vehicle with the hydrodynamic forces decoupled from the rigid body dynamics. These equations can be written as

$$\tau_c = M_{\mathrm{RB}}\dot{v} + C_{\mathrm{RB}}(v)v + f_{\mathrm{D}} + f_{\mathrm{N}}, \tag{3}$$

where M_{RB} and $C_{\mathrm{RB}}(v) \in \mathbb{R}^{6\times6}$ denote the inertial and Coriolis/centrifugal matrices associated with the rigid body, $f_{\mathrm{D}} \in \mathbb{R}^6$ represents the hydrodynamic forces and moments, and $f_{\mathrm{N}} \in \mathbb{R}^6$ represents the unmodeled disturbance forces and moments acting on the vehicle. Additionally, the control forces can be defined as the sum of the feedback forces and estimated hydrodynamic forces (from a sensory system). By defining the forces in this manner, the hydrodynamic forces act as a feedforward term, greatly improving the performance of the vehicle (Xu & Mohseni, 2014). Figure 1 shows simulation results comparing the position errors (x, y, and yaw) of a vehicle with a lateral line system as a feedforward control element against the performance of a vehicle without a lateral line system. The lateral line system allows the vehicle to sense hydrodynamic disturbances and compensate for them, improving the tracking performance. The major source of the remaining error is due to localization errors. The feedforward lateral line system is able to improve tracking performance of the vehicle by 20–50% (see Xu & Mohseni, 2014, for additional details).

FIGURE 1

Comparison of simulated performance of underwater vehicle (a) with lateral line and (b) without lateral line system. Originally presented in Xu and Mohseni (2014). The x, y, and *yaw* errors of the vehicle in the global coordinate frame are represented by e_{11}, e_{12}, and e_{13}, respectively.

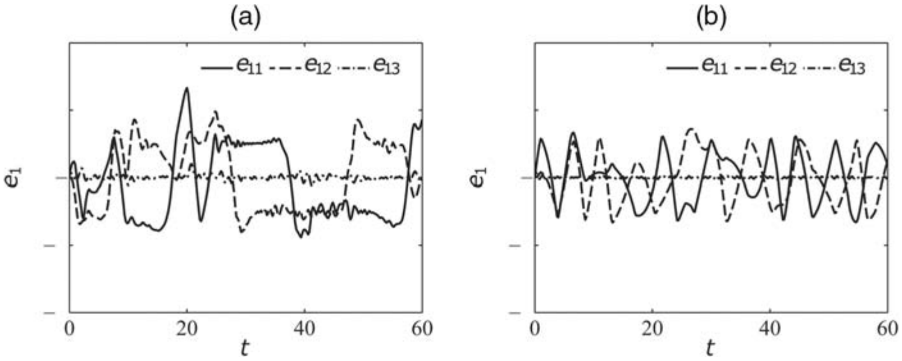

Bio-inspired Vehicle: CephaloBot

Our group has worked on several generations of bio-inspired underwater vehicles including five generations of mother vehicles (Krieg et al., 2011) and two generations of daughter vehicles (Song et al., 2016). Our group emphasizes research in hierarchical, swarm-based control (Song et al., 2017) with capable mother vehicles supporting smaller daughter vehicles. The goal is to have a distributed, mobile sensor network.

The current generation of mother vehicles, named CephaloBot, is a hybrid class vehicle that combines a rear propeller and four biologically inspired squid thrusters (Krieg et al., 2011; Mohseni, 2004). The squid thrusters, also called vortex ring thrusters (VRTs), allow CephaloBot to have full control authority in the horizontal plane without the need for control surfaces, enabling sway and zero-radius turning maneuvers while maintaining a streamlined, low-drag shape.

Our group has extensively modeled the dynamics of the thrusters (Krieg & Mohseni, 2008, 2010, 2015). For our purposes, we present the model of the average force produced by the thrusters as a function of the actuation frequency f, actuator stroke ratio L/D, and the diameter of the nozzle D, given as

$$F = \frac{\rho\pi^3}{8}\left(g + \frac{k_2^* - k_1^*}{4}\right)\left(\frac{L}{D}\right)^2 D^4 f^2,$$

where ρ is the density of water. Exact methods for calculating instantaneous force are described in Krieg and Mohseni (2015). A pair of the squid thrusters is located on each side of the hull about 0.31 m fore and aft of the center of mass, as shown in Figure 2.

Modular Lateral Line Design

Previous studies have shown that an artificial lateral line system with statically placed sensors is quite effective for disturbance rejection and wall detection (Xu & Mohseni, 2014, 2017; Nelson & Mohseni, 2017). Photographs of these setups are presented in Figures 3(a) and 3(b). However, implementing a similar system on a vehicle would require costly and difficult modifications to the hull of the vehicle. To address this issue, we present a modular lateral line system that fits around an existing vehicle like a shell without the need for hull modifications (this system is shown in Figure 3(c)). The modular lateral line system features a centralized processor and distributed sensor modules, each containing a pair of sensors. The number of sensors can be increased or decreased as needed based on the vehicle geometry and sensing needs of the mission. A 3-D printed scaffolding holds the sensor modules in place. The sensor modules and scaffolding use interchangeable parts allowing for additional flexibility when assembling the system. The central processor collects data simultaneously from all the sensors, processes the data, and then sends the fused data to the vehicle. In this paper, we show that such a system can be used to calculate the hydrodynamic forces acting on a rigid body, and these results could be available for real-time vehicle control.

Sensor Module Design

We designed the sensor modules to be self-contained, replaceable, and waterproof. Each of the sensor modules contains an in-house developed sensor circuit embedded in elastomer. The sensor circuit contains a pair of differential pressure sensors, digitally tunable low-pass filters, and ADCs. The elastomer protects and waterproofs the sensor circuits; the sensor modules are molded to easily and seamlessly integrate with the 3-D printed scaffolding.

FIGURE 2

Photograph of our in-house designed and built autonomous underwater vehicle CephaloBot. The vehicle acts as an autonomous, mobile sensor platform capable of completing a diverse set of missions. CephaloBot features four bio-inspired VRTs (two can be seen in the photo facing the camera) that allow the vehicle to have full control authority in the horizontal plane without having control surfaces.

FIGURE 3

Photographs of three of the lateral line setups we have built: (a) the force estimation system with statically placed sensors, (b) the wall detection system with statically placed sensors, and (c) the modular lateral line system.

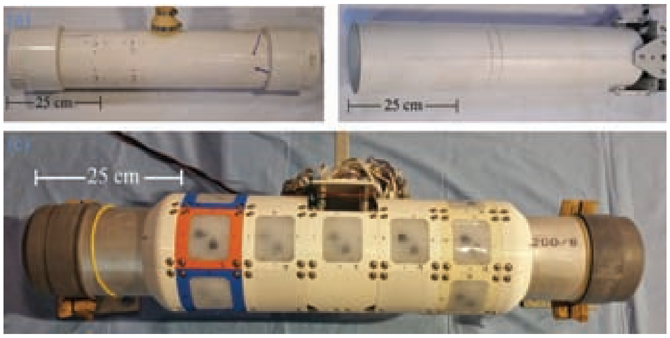

The sensors we used in the sensor modules are Freescale Semiconductor MPXV7002DP differential pressure sensors. The differential pressure sensors provide an acceptable performance trade-off between accuracy, sensitivity, sensing range, size, and cost. In contrast to most other groups, we use differential pressure sensors instead of absolute or gauge pressure sensors. Differential pressure sensors tend to have a much higher sensitivity and much smaller sensing range than gauge or absolute pressure sensors. However, the range of a differential pressure sensor is not equivalent to the range of a gauge or absolute pressure sensor. The range of gauge and absolute pressure sensors is partially saturated by the atmospheric pressure and hydrostatic pressure, whereas the range of differential pressure sensors is only affected by the relative pressure difference between the two ports. Of course, one potential drawback of differential pressure sensors is that they only provide the relative pressure difference across the two ports. However, for the purpose of hydrodynamic force estimation, the static pressure drops out during integration, and the lack of an absolute pressure measurement is unnecessary.

The MPXV7002DP has a sensitivity of 1.0 V/kPa, a sensing range of ±2kPa, and a typical accuracy of ±0.1 kPa. The sensor modules contain 12-bit ADCs, giving them a resolution of 1.22 Pa. To improve the performance of the system, we implemented a first-order low-pass filter with a digital potentiometer into the sensor module. The microprocessor tunes the resistance of the potentiometer to set the cutoff frequency of the filter based on the sampling frequency to remove aliasing. Additionally, the software calibrates the sensors at a steady-state pressure to remove inaccuracies caused by sensor drift. Further filtering is performed digitally, and we are able to achieve an accuracy of around ±1 Pa. The peak hydrodynamic pressure difference measured during validation testing was around 200 Pa, well above the accuracy threshold.

Figure 4 shows the sensor module manufacturing process. Figures 4(a) and 4(b) show the mold we designed for the manufacturing process. The mold holds the sensor boards, fasteners, and sensor tubing. The manufacturing process is as follows. First, the sensor board is prepared for the molding process. All necessary components and connectors are soldered to the board, and 1/8-inch outer-diameter clear PVC tubing is attached to the nozzles of the pressure sensors. Next, the sensor module mold is coated with mold release to aid in the removal of the cured elastomer. The circuit board is then placed at the bottom of the mold, and the vinyl tubing is routed through holes at the bottom of the mold (see Figures 4(c) and 4(d)); this tubing allows the sensors to measure pressure at the surface of the module. Care is taken to ensure that the lengths of the tubes are equal. Screws are attached to the top of the mold to suspend fasteners in the elastomer as it cures. The fasteners are later used to mechanically attach the sensor modules to the scaffolding. Additional screws are used to clamp the two halves of the mold together during the molding process. Finally, elastomer is poured into the mold so that it covers the circuit and fasteners (as shown in Figure 4(e)). The elastomer acts as an insulating layer for the sensor boards, waterproofing them and protecting them from damage. After the elastomer cures, the sensor module is removed from the mold, excess elastomer is removed, and the tubes are cut flush with the surface of the module. Figure 4(e) shows the finished sensor module, and Figure 5 shows a schematic

FIGURE 4

Photographs of the sensor module manufacturing process. Photos of the top (a) and bottom (b) pieces of the 3-D printed mold used during the manufacturing process. (c) The sensor board placed in the mold. (d) A close-up of the sensor board and vinyl tubing. (e) The curing elastomer. (f) The finished module.

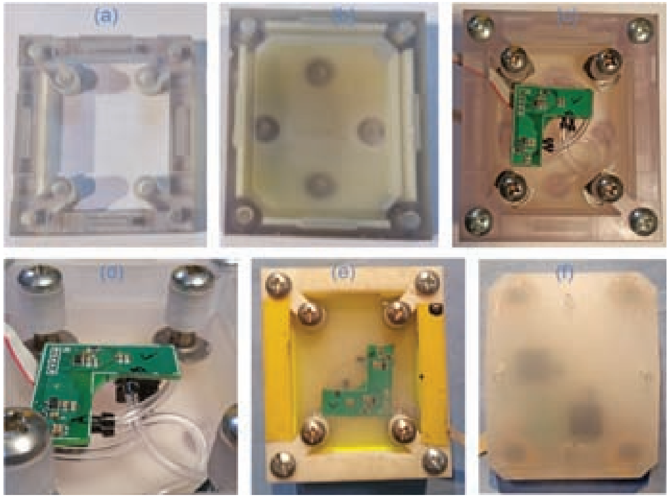

FIGURE 5

Lateral line sensor module. (a) Photo of the top of the sensor module. (b) Photo of the bottom of the sensor module. (c) Schematic of the sensor module.

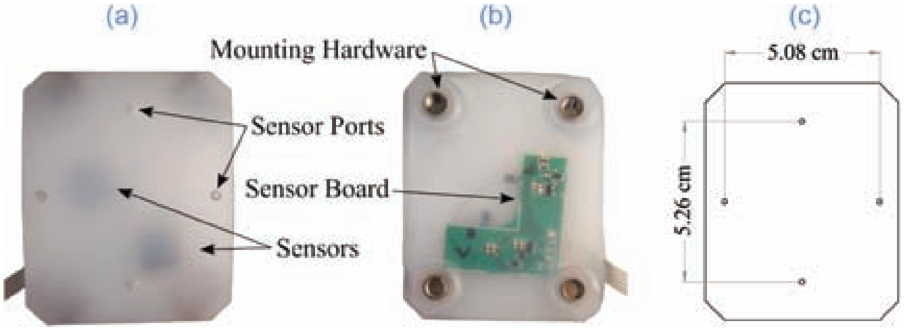

of the sensor module along with labeled photographs of the top and bottom of the sensor module.

Sensor Placement

As shown in Figure 5, each sensor module contains two differential sensors. The four sensor ports are routed to the surface of the modules via vinyl tubing. Each set of sensor ports is laid out so that the port separation is in line with the circumferential and longitudinal axes of the body. This simplifies the interpolation of the pressure distribution by ensuring that the measurements are along different coordinate axes. Calculating the distributed pressure across the surface of the body presents an interesting challenge. Enough sensors must be used so that all useful features of the pressure distribution are accurately captured; at the same time, the port separation must be large enough that the change in pressure can be detected by the sensors.

For our vehicle, we approximated the shape of the body as a cylinder. Bernoulli's equations allow us to approximate the hydrodynamic pressure around a circular cylinder in cross-flow as (Milne-Thompson, 1968)

$$P_{\mathrm{D}}(\theta) = \frac{1}{2}\rho U^2(2\cos 2\theta - 1) + P_\infty \qquad (4)$$

where ρ is the density of the fluid, U is the freestream velocity, θ is the angle around the circumference of the cylinder, and P_∞ is the static pressure of the freestream. This equation only applies in the case of an inviscid, incompressible fluid. However, for a streamlined vehicle like ours, we do not expect massive separations, and the application of inviscid theory might be tolerated; thus, the potential flow model can be used as a guideline choosing a minimum number of sensors. The dominant (in fact, only) wave number, or spatial frequency, present in Equation (4) is the wave number 2. According to the Nyquist Theorem, a signal must be sampled at least twice its highest frequency to avoid aliasing or loss of information. Thus, we ideally want more than four sensors distributed around the circumference of the cylinder (i.e., more sensors than twice the spatial frequency). We chose to use six sensors placed around the circumference of the cylinder, providing additional robustness to the system without greatly increasing the complexity of the system.

An analytical model of the flow over the vehicle in the longitudinal direction is much more difficult to derive than the model of the flow around the circumference of the body. We placed five sensor modules in the longitudinal direction on both sides of the cylinder. We will validate the accuracy of such a sensor distribution for force measurement in the Experimental Setup section.

Sensor Port Separation

One interesting design decision when using differential pressure sensors is the port separation. The distance between the ports influences the sensitivity of the system (Ren & Mohseni, 2012). If the pressure between the ports is monotonically increasing (or decreasing), then increasing the separation of the ports increases (decreases) the measured pressure difference. Similarly, decreasing the port separation will decrease the amplitude of the measured signal. If the pressure signal between the ports is not a monotonic function, then sensors are not able to measure all the information present in the signal (essentially, the signal is being aliased), and increasing the port separation only increases the amount of lost information. To ensure aliasing does not occur, a suitable number and distribution of sensors must be chosen based on the desired spatial recovery of the flow features. The main objective becomes to optimize the port separation to maximize the signal-to-noise ratio while keeping the port separation small enough to avoid saturation of the sensor and to avoid spatial aliasing of the sampled pressure distribution.

An additional concern for the port spacing is the vertical spacing with respect to gravity. The hydrostatic pressure difference from the height of the water column will cause part of the sensors' range to become saturated. Recall that the hydrostatic pressure of a fluid is given by

$$p = \rho g h$$

where ρ is the density of the fluid, g is the acceleration due to gravity (9.8 $\mathrm{m/s^2}$), and h is the height of the fluid column. Therefore, the hydrostatic pressure in water increases at a rate of about 9.8 kPa/m. Our sensors have a port separation of 5.26 cm corresponding to an angle of about 30°. The static pressure difference for the corresponding change of depth is about 500 Pa (i.e., if the sensor ports were distributed the maximum vertical distance).

Additionally, we use the model in Equation (4) to estimate the maximum dynamic pressure difference for a given velocity. By approximating the pressure gradient as the pressure difference divided by the port separation, that is,

$$\frac{dP(\theta)}{d\theta} \approx \frac{\Delta \mathrm{P}(\theta)}{\Delta \theta},$$

we can arrive at the equation

$$\Delta P(\theta) \approx -2 p U^2 \sin(2\theta) \Delta \theta, \qquad (5)$$

which has two maxima and two minima occurring when $\sin(2\theta) = \mp 1$, respectively. That is, the maximum differential dynamic pressure is simply a function of the peak-to-peak pressure modified by the port spacing, $\Delta\theta$. Another observation of the above analysis is that there are four "dead zone" locations, locations where the model predicts a zero pressure difference regardless of port separation and flow velocity. These areas correspond to the locations of the peak pressure (stagnation points), that is, the front and back of the cylinder, and locations of minimum pressure at the top and bottom of the cylinder. Of course, this only applies to certain ideal cases; in a nonideal flow, the cylinder will have vortex shedding and 3-D effects causing the pressure distribution on the trailing edge to have additional terms. If characterizing the shedding is of interest, additional sensors placed at the predicted shedding location will improve the accuracy of the pressure profile estimation. We chose to distribute the sensors equally around the cylinder starting at the separation point and at each location 60° apart (as shown in Figure 6(b)). This allows us to measure the pressure difference at the separation points with the front and back sensors, and the remaining four sensors are distributed near the locations of greatest dynamic pressure difference.

FIGURE 6

Representation of port distribution of the sensor modules around the cylinder. (a) An individual sensor module and radial port distribution. (b) The radial spacing of the sensor modules.

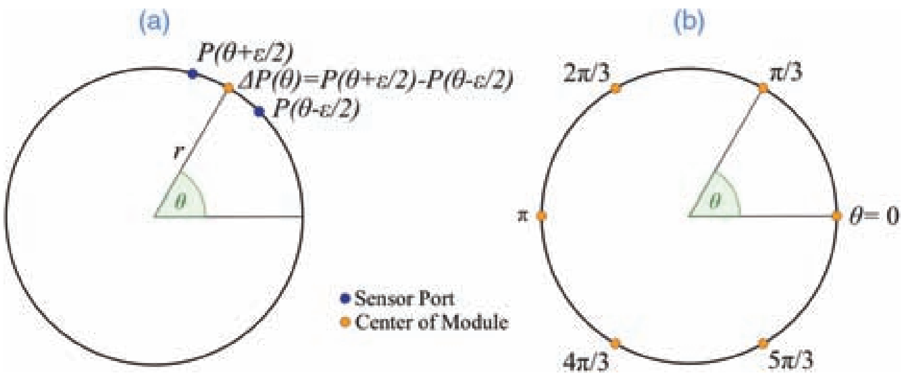

The total pressure difference is the sum of the static pressure difference and the dynamic pressure difference. Considering a velocity of 0.5 m/s (the maximum for the vehicle), the maximum dynamic pressure difference (calculated using Equation (5)) is about 250 Pa. Thus, the sum of the static and dynamic differential pressures is 750 Pa, within the range of the differential pressure sensors, ±2 kPa. We measured the standard deviation of the noise of our sensors to be about 0.4 Pa, which is well below the expected amplitude of the dynamic pressure difference. Thus, expected pressure difference falls within the sensor's range, and the magnitude of the signal should be much higher than the sensor noise.

Electronic System Architecture

We chose a Microchip dsPIC30F6010A to function as the central processing unit for the lateral line system. The microprocessor communicates with the sensor modules using a parallel implementation of the $\mathrm{I^2C}$ (Inter-Integrated Circuit) communication protocol (see Figure 7 for diagrams of the standard and parallel $\mathrm{I^2C}$ architectures). Typically, $\mathrm{I^2C}$ supports multiple devices on a single pair of wires (a clock line and a data line),

FIGURE 7

Schematic of (a) standard I^2C architecture and (b) parallel I^2C architecture. The parallel architecture requires an additional data line for each additional sensor added to the system; however, it also allows all sensors to be sampled simultaneously. In the diagrams, the clock line is defined as SCL and the data lines are defined as SDA or SDA *X*, where *X* is the corresponding sensor in the parallel architecture.

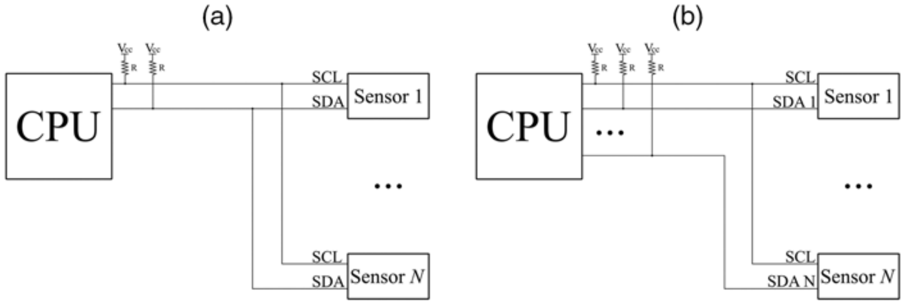

with only a single device being able to communicate at a time. Our parallel implementation of I^2C allows the master to communicate with multiple peripherals simultaneously. Each sensor has a separate data line, and all the ADCs have identical addresses. As with the standard I^2C protocol, all devices share a single clock line. The data lines are connected to individual general-purpose input/output (GPIO) pins on the central processor. The processor uses bit-banging techniques to emulate the functionality of I^2C hardware on the GPIO pins. When the processor initiates a data transfer, it sends out a read request to all of the ADCs simultaneously, thereby ensuring that all of the pressure sensors are sampled simultaneously, the primary motivation for implementing this architecture. The disadvantage of this parallel implementation of I^2C is scalability: as the number of sensors increases, not only does the number of required wires and GPIO ports increase, but also the baud rate decreases as the processor must sample from additional sensors. However, a similar issue arises for standard I^2C as additional sensors require additional data transactions to be initiated. Overall, the parallel I^2C architecture should be more efficient than the standard architecture, with the added benefit of guaranteeing that the data are sampled simultaneously.

As with the sensor modules, we sealed the processor in elastomer to protect and waterproof it. We routed the necessary communication and power wires outside the elastomer and to the sensor modules. An Ethernet cable was connected to the processor board and serves as the main communication line and power lines. This Ethernet cable is then connected to a PC or the autonomous underwater vehicle depending on the test scenario. The central processor is able to collect data from all the sensors, process them, and send data to the vehicle at a frequency of about 30 Hz.

Force Estimation Algorithm

One major benefit of implementing the lateral line system is that it allows the hydrodynamic forces acting on a body to be calculated from the pressure measurements. These sensors measure the pressure difference between their ports rather than absolute pressure measurements. By incorporating knowledge of the sensor geometry, the pressure gradient over the surface of the body is calculated. Spatial integration of the pressure gradient yields the pressure distribution over the surface. Integrating the hydrodynamic pressure distribution over the surface of the body yields the hydrodynamic forces.

Due to the simple geometry of the vehicle, we approximate the body of the vehicle as a cylinder. Recall that the gradient in cylindrical coordinates is defined as

$$\nabla \equiv \hat{r}\frac{\partial}{\partial r} + \hat{\theta}\frac{1}{r}\frac{\partial}{\partial \theta} + \hat{z}\frac{\partial}{\partial z},$$

where the notation $\hat{u}$ denotes that the vector u is a unit vector. Because we are only concerned with the pressure distribution over the surface of the body, the partial derivative with respect to the radial component drops out. Additionally, we can examine the circumferential and longitudinal components independently. The pressure gradient around circumference of the cylinder, that is, holding the pressure constant with respect to the r and z axes, is given by

$$\nabla P(\theta) = \frac{1}{r}\frac{\partial P(\theta)}{\partial \theta} \approx \frac{\Delta P}{\mathrm{r}\Delta \theta},$$

where ΔP is the pressure difference measured by the sensors and $r\Delta\theta$ is the separation between the sensor ports. We calculate the pressure gradient at a given point from the pressure sensor measurement and port separation. Because the domain is periodic, the Shannon-Whitaker interpolation (Shannon, 1949) formula can be used to construct a continuous time pressure gradient. The interpolation formula is given as

$$x(t) = \sum_{n=-\infty}^{\infty} x[n] sinc\left(\frac{t-nT}{T}\right).$$

where $x(t)$ is a continuous valued function, $x[n]$ is a discrete valued function, T is the sampling period, and *sinc* is the normalized cardinal sine function, that is

$$sinc(x) = \frac{\sin(\pi x)}{\pi x}.$$

The pressure gradient can be broken up into two components, a static component and a dynamic component. After removing the static component from the total pressure gradient, the dynamic pressure gradient can then be integrated to calculate the dynamic pressure distribution, that is,

$$P_D(\theta) = \int_0^{2\pi} \frac{\partial P_{\mathrm{D}}(\theta)}{\partial \theta} \mathrm{d}\theta.$$

This distribution can then be used to calculate the forces acting on the cylinder. The hydrodynamic force acting on the surface of a body ignoring shear stress is

$$F_{\mathrm{D}} = \int_S P_{\mathrm{D}} \hat{n} \, dS, \tag{6}$$

where $\hat{n}$ is the unit vector normal to the surface S defined positive inward and P_{D} is the dynamic pressure. For a cylinder of length l and radius r, if the pressure is constant in the z direction, the above equation simplifies to

$$F_{\mathrm{D}} \approx r \int_0^l dz \int_0^{2\pi} P_D(\theta) \hat{n} \, d\theta, \ \ \hat{n} = [\cos\theta, \sin\theta, 0],$$

where $F_{\mathrm{D}} \in \mathbb{R}^3$ has components in Cartesian coordinates.

The above formulation is only valid if the pressure distribution is not changing along the z axis of the cylindrical coordinates (which lines up with the x axis of the body frame of the vehicle). For a pressure distribution that is changing in the z direction, a general formulation can be derived from Equation (6). In this case, our vehicle can be approximated as a cylinder with a hemisphere nose section. The pressure distribution can be estimated using similar techniques as presented above, and the forces can be calculated by integrating the pressure distribution over the surface of the vehicle. Additional sensors will need to be placed at the front and back of the vehicle (relative to x body axis) to form a closed distribution of sensors.

The force calculation algorithm presented in this paper was derived based on the geometry of the system. For other vehicle geometries and sensor layouts, the derivation of the force estimation algorithm from Equation (6) will have to be repeated with the correct geometry. For a general geometry, where analytic pressure distribution estimates are not available, one might resort to numerical calculation in order to identify optimal sensor locations.

Experiments

Experimental Setup

The experimental validation was performed in a large testing tank (see Figure 8(a)) with a diameter of 8 m, a depth of 4.5 m, and a total volume of about 225,000 L. A cart (shown in Figure 8(b)) connects to an I-beam running above the tank; this cart constrains the movement of the lateral line system to one dimension, which is normal to the surface of the cylinder, creating a cross-flow over the cylinder. The lateral line sensors measure the pressure over the surface of the cylinder created by the movement of the system. The embedded processor collects the data from all of the sensors and sends the resulting information to a computer logging the data. When the system is integrated with the vehicle, the processor could instead send the fused data directly to the vehicle without the need of an intermediate computer. An aluminum rod connects the lateral line system to the cart. Four sets of four strain gauges are mounted to the rod in a standard full-bridge circuit; these sensors measure the forces and moments acting on the rod. HX711 load cell amplifiers from Avia Semiconductor are used to measure the voltage across the bridge. The strain gauges are calibrated by applying known forces and moments to the rod and measuring the response. Six motion capture cameras are located at the bottom of the tank and measure the cylinder's position, velocity, and acceleration. After calibration, this system is able to position measurements with millimeter accuracy at a sampling

FIGURE 8

Lateral line test facility. (a) Photo of the large testing tank. (b) Schematics of the cart that attaches to the I-beam running along the top of the tank. The lateral line system by an aluminum rod to the cart and towed through the tank. The cart moves along the I-beam, restricting the movement of the system.

rate of 100 Hz. The inertial forces of the cylinder are calculated from the acceleration of the cylinder.

Experimental Validation

To validate the force estimation algorithm and modular lateral line system, we towed the lateral line setup (shown in Figure 3(c)) through water and compared the hydrodynamic forces calculated from the pressure distribution measured by the lateral line pressure sensors to a reference force. Theoretically, the sum of the hydrodynamic and reaction forces on the rod should equal the inertial forces. We use this fact to calculate a reference hydrodynamic force that we compare against the hydrodynamic force estimated by the lateral line system.

We experimentally validated the system for several cases; a sample result comparing the reference hydrodynamic force with the hydrodynamic force calculated from the lateral line pressure data is presented in Figure 8. As described in the Sensor Placement and Force Algorithm sections, two rings of six sensors encompass the radial direction of the cylinder and are used to measure the pressure gradient over the cylinder. Before the pressure gradient is integrated, the measurements of the six sensors are up-sampled using a Fast Fourier Transform (FFT) interpolation algorithm (essentially a discrete version of the Whittaker-Shannon interpolation formula). The up-sampled signal is then integrated twice to calculate the drag forces acting on the cylinder in the direction of travel.

As seen in Figure 9, six sensors are able to capture the majority of the hydrodynamic information required to predict the forces acting on the cylinder. As we discussed in the Sensor Placement section, theoretically, the pressure is dominated by wave number 2. This suggests that as few as four sensors could be used to capture the majority of the information; however, the quality of the results would presumably suffer. Likewise, adding additional sensors could presumably increase the quality of the estimated force, at the expense of increasing the computational complexity of the algorithm.

The pressure gradient at the instance of the peak velocity is shown in Figure 10(a). The sensor measurements are shown with blue asterisks, and the line shows the interpolated pressure gradient using Fourier interpolation. The interpolated pressure gradient is integrated resulting in the pressure distribution shown in Figure 10(b). There is a noticeable pressure asymmetry between the front and back of the cylinder. This drop in pressure is caused by the hydrodynamic forces acting unevenly on the cylinder resulting in drag forces on the cylinder. In Figure 10(b), the rear stagnation point is located at about $\theta = 190°$. We believe asymmetric vortex shedding at this instance of time has caused the movement of the station point from $\theta = 180°$ to about $\theta = 190°$. The vortex shedding behind the cylinder causes the stagnation point to oscillate around the point $\theta = 180°$.

FIGURE 9

Results of validation of the modular lateral line system. (a) Velocity of the cylinder measured by the motion capture system. (b) Hydrodynamic force calculated by the lateral line compared to a reference force calculated by subtracting the reaction force on the rod measured independently by the inertial force.

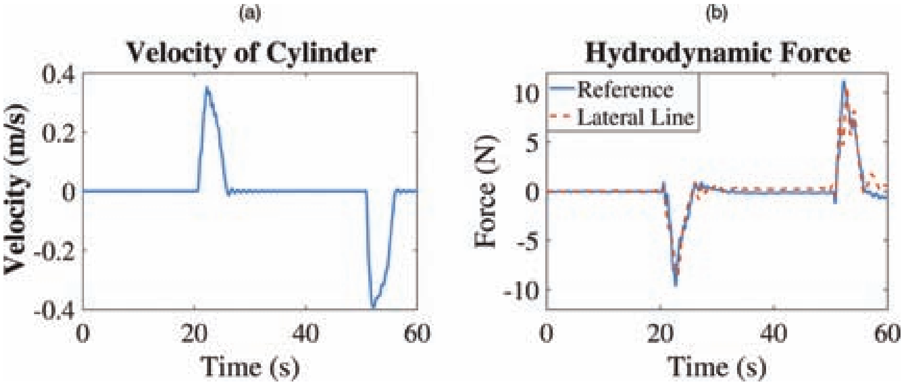

FIGURE 10

The pressure and pressure gradient distributions over the cylinder at the instance of the peak velocity of the cylinder. (a) The pressure gradient distribution is interpolated from the measurements of six sensors (shown by asterisks) using Fourier interpolation. (b) The pressure distribution is calculated by integrating the pressure gradient around the cylinder.

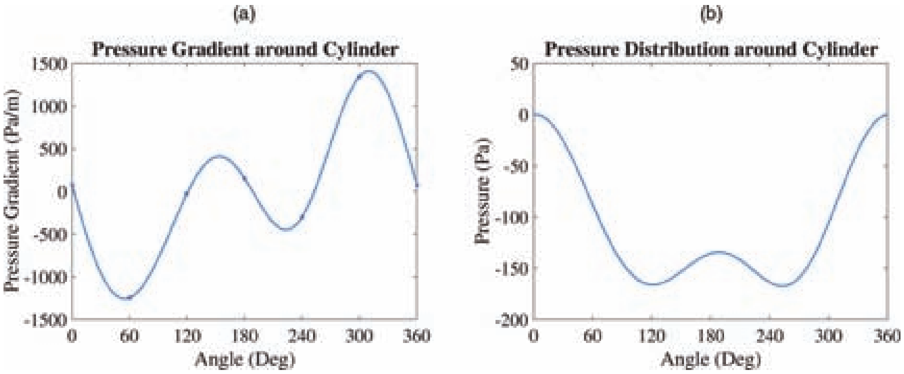

In the reported test, we isolated the movement of the cylinder to the *y* body axis (i.e., normal to the surface of the cylinder) such that the flow over the cylinder is uniform with respect to the *x* body axis. This movement isolates the hydrodynamic forces so they are primarily acting along this axis, greatly simplifying the calculations of the forces. However, in the presence of a nonuniform flow, the sensors distributed along the *x* body axis could be used to calculate the pressure distribution along the *x* axis from which the moments acting on the cylinder could be estimated.

Conclusion

In this paper, we present a modular lateral line sensory system for improving control strategies for autonomous underwater vehicle testing. The modular lateral line was designed to be implemented as a shell surrounding the vehicle in order to avoid costly modification to the hull of the vehicle. The design and manufacturing of this modular lateral line system were discussed in detail; although this process was tailored to CephaloBot, it can be easily adapted to additional vehicles. A force estimation algorithm was developed for this system and experimentally validated, showing that the lateral line can be used to measure hydrodynamic forces acting on the body.

Future work includes implementing this system on an underwater vehicle and showing the improved control performance. The current setup will work for calculating the hydrodynamic forces in the *y* body frame, and the initial investigation will pursue that course of action. Additionally, we plan to expand our current system to include additional sensors to cover the entire vehicle, specifically around the nose cone and rear thruster. We also plan to develop a soft skin with pressure sensing capabilities in order to reduce the overall impact of the lateral line system on the profile of the vehicle.

Acknowledgments

The authors would like to gratefully acknowledge partial support from the Office of Naval Research through Dr. T. McKenna's program and the National Science Foundation for funding this project.

Corresponding Author:

Kamran Mohseni
University of Florida
NEB Room 141
Gainesville, FL 32611
Email: mohseni@ufl.edu

References

Abdulsadda, A.T., & Tan, X. 2013. Underwater tracking of a moving dipole source using an artificial lateral line: Algorithm and experimental validation with ionic polymer–metal composite flow sensors. Smart Mater Struct. 22(4):045010. https://doi.org/10.1088/0964-1726/22/4/045010.

Akanyeti, O., Chambers, L.D., Ježov, J., Brown, J., Venturelli, R., Kruusmaa, M., … Fiorini, P. 2013. Self-motion effects on hydrodynamic pressure sensing: Part I. Forward–backward motion. Bioinspir Biomim. 8(2):026001. https://doi.org/10.1088/1748-3182/8/2/026001.

Blaxter, J.H.S. 1987. Structure and development of the lateral line. Biol Rev. 62(4):471-514. https://doi.org/10.1111/j.1469-185X.1987.tb01638.x.

Bleckmann, H. 2008. Peripheral and central processing of lateral line information. J Comp Physiol A. 194(2):145-58. https://doi.org/10.1007/s00359-007-0282-2.

Chambers, L.D., Akanyeti, O., Venturelli, R., Ježov, J., Brown, J., Kruusmaa, M., … Megill, W.M. 2014. A fish perspective: detecting flow features while moving using an artificial lateral line in steady and unsteady flow. J R Soc Interface. 11(99):20140467. https://doi.org/10.1098/rsif.2014.0467.

Coombs, S. 2001. Smart skins: Information processing by lateral line flow sensors. Auton Robots. 11(3):255-61. https://doi.org/10.1023/A:1012491007495.

Coombs, S., Braun, C.B., & Donovan, B. 2001. The orienting response of Lake Michigan mottled sculpin is mediated by canal neuromasts. J Exp Biol. 204(2):337-48.

Coombs, S., & Montgomery, J. 1994. Function and evolution of superficial neuromasts in an Antarctic notothenioid fish. Brain Behav Evol. 44(6):287-98. https://doi.org/10.1159/000113590.

Dagamesh, A., Wiegerink, R., Lammerink, T., & Krijnen, G. 2013. Imaging dipole flow sources using an artificial lateral-line system made of biomimetic hair flow sensors. J R Soc Interface. 10(83):20130162. https://doi.org/10.1098/rsif.2013.0162.

Devries, L., Lagor, F.D., Lei, H., Tan, X., & Paley, D.A. 2015. Distributed flow estimation and closed-loop control of an underwater vehicle with a multi-modal artificial lateral line. Bioinspir Biomim. 10(2):025002. https://doi.org/10.1088/1748-3190/10/2/025002.

Fan, Z., Chen, J., Zou, J., Bullen, D., Liu, C., & Delcomyn, F. 2002. Design and fabrication of artificial lateral line flow sensors. J Micromech Microeng. 12(5):655. https://doi.org/10.1088/0960-1317/12/5/322.

Fernandez, V.I., Maertens, A., Yaul, F.M., Dahl, J., Lang, J.H., & Triantafyllou, M.S. 2011. Lateral-line-inspired sensor arrays for navigation and object identification. Mar Technol Soc J. 45(4):130-46. https://doi.org/10.4031/MTSJ.45.4.20.

Fossen, T.I. 2011. Handbook of Marine Craft and Hydrodynamics and Motion Control. Chichester, UK: John Wiley & Sons. 575 p. https://doi.org/10.1002/9781119994138.

Gao, A., & Triantafyllou, M.S. 2012. Bio-inspired pressure sensing for active yaw control of underwater vehicles. In: Oceans Conference 2012, p. 06404844. Hampton Roads, VA: IEEE. https://doi.org/10.1109/OCEANS.2012.6404844.

Klein, A., & Bleckmann, H. 2011. Determination of object position, vortex shedding frequency and flow velocity using artificial lateral line canals. Beilstein J Nanotech. 2:276-83. https://doi.org/10.3762/bjnano.2.32.

Kottapalli, A.G., Asadnia, M., Miao, J.M., Barbastathis, G., & Triantafyllou, M.S. 2012. A flexible liquid crystal polymer MEMS pressure sensor array for fish-like underwater sensing. Smart Mater Struct. 21(11):115030. https://doi.org/10.1088/0964-1726/21/11/115030.

Kottapalli, A.G.P., Asadnia, M., Miao, J., & Triantafyllou, M. 2014. Touch at a distance sensing: lateral-line inspired MEMS flow sensors. Bioinspir Biomim. 9(4):046011. https://doi.org/10.1088/1748-3182/9/4/046011.

Kottapalli, A.G.P., Tan, C.W., Olfatnia, M., Miao, J.M., Barbastathis, G., & Triantafyllou, M. 2011. A liquid crystal polymer membrane MEMS sensor for flow rate and flow direction sensing applications. J Micromech Microeng. 21(8):085006. https://doi.org/10.1088/0960-1317/21/8/085006.

Krieg, M., Klein, P., Hodgkinson, R., & Mohseni, K. 2011. A hybrid class underwater vehicle: bioinspired propulsion, embedded system, and acoustic communication and localization system. Mar Technol Soc J. 45(4):152-64. http://dx.doi.org/10.4031/mtsj.45.4.11.

Krieg, M., & Mohseni, K. 2008. Thrust characterization of pulsatile vortex ring generators for locomotion of underwater robots. IEEE J Ocean Eng. 33(2):123-32. http://dx.doi.org/10.1109/JOE.2008.920171.

Krieg, M., & Mohseni, K. 2010. Dynamic modeling and control of biologically inspired vortex ring thrusters for underwater robot locomotion. IEEE T Robot. 26(3):542-54. https://doi.org/10.1109/TRO.2010.2046069.

Krieg, M., & Mohseni, K. 2015. Pressure and work analysis of unsteady, deformable, axisymmetric, jet producing cavity bodies. J Fluid Mech. 793:337-68. https://doi.org/10.1017/jfm.2015.120.

Kroese, A.B., & Schellart, N.A. 1992. Velocity-and acceleration-sensitive units in the trunk lateral line of the trout. J Neurophysiol. 68(6):2212-21.

Kroese, A.B., Van der Zalm, J.M., & Van den Bercken, J. 1978. Frequency response of the lateral-line organ of Xenopus laevis. Pfluegers Archiv. 375(2):167-75. https://doi.org/10.1007/BF00584240.

McConney, M.E., Chen, N., Lu, D., Hu, H.A., Coombs, S., Liu, C., & Tsukruk, V.V. 2009. Biologically inspired design of hydrogel-capped hair sensors for enhanced underwater flow detection. Soft Matter. 5(2):292-5. https://doi.org/10.1039/B808839J.

Milne-Thompson, L.M. 1968. Theoretical Hydrodynamics. New York, NY: Macmillan Press. 743 p. https://doi.org/10.1007/978-1-349-00517-8.

Mohseni, K. 2004. Zero-mass pulsatile jets for unmanned underwater vehicle maneuvering. In: AIAA 3rd "Unmanned Unlimited" Technical Conference, Workshop and Exhibit, pp. 2004-6386. Chicago, IL. Publisher: American Institute of Aeronautics and Astronautics (AIAA). https://doi.org/10.2514/6.2004-6386.

Montgomery, J.C., Baker, C.F., & Carton, A.G. 1997. The lateral line can mediate rheotaxis in fish. Nature. 389(6654):960. https://doi.org/10.1038/40135.

Montgomery, J.C., Carton, G., Voigt, R., Baker, C., & Diebel, C. 2000. Sensory processing of water currents by fishes. Philos T R Soc B. 355(1401):1325-7. https://doi.org/10.1098/rstb.2000.0693.

Montgomery, J.C., & MacDonald, J.A. 1987. Sensory tuning of lateral line receptors in Antarctic fish to the movements of planktonic prey. Science. 235:195-7. https://doi.org/10.1126/science.235.4785.195.

Muñz, H. 1989. Functional organization of the lateral line periphery. In: The Mechanosensory Lateral Line, eds. Coombs, S., Görner, P., & Münz, H., 285-97. New York, NY: Springer. https://doi.org/10.1007/978-1-4612-3560-6_14.

Nelson, K., & Mohseni, K. 2017. An artificial fish lateral line sensory system composed of modular pressure sensor blocks. In: 2017 IEEE International Conference on Robotics and Automation (ICRA). Singapore: IEEE. http://dx.doi.org/10.1109/ICRA.2017.7989569.

Pitcher, T.J., Partridge, B.L., & Wardle, C.S. 1976. A blind fish can school. Science. 194(4268):963-5. https://doi.org/10.1126/science.982056.

Pohlmann, K., Atema, J., & Breithaupt, T. 2004. The importance of the lateral line in nocturnal predation of piscivorous catfish. J Exp Biol. 207(17):2971-8. https://doi.org/10.1242/jeb.01129.

Ren, Z., & Mohseni, K. 2012. A model of the lateral line of fish for vortex sensing. Bioinspir Biomim. 7(3):036016. https://doi.org/10.1088/1748-3182/7/3/036016.

Ren, Z., & Mohseni, K. 2014. Wall detection by lateral line sensory system of fish. In: 52nd Aerospace Sciences Meeting, AIAA SciTech Forum (AIAA 2014-0072). National Harbor, MD: AIAA. https://doi.org/10.2514/6.2014-0072.

Satou, M., Takeuchi, H.A., Nishii, J., Tanabe, M., Kitamura, S., Okumoto, N., & Iwata, M. 1994. Behavioral and electrophysiological evidences that the lateral line is involved in the intersexual vibrational communication of the himé salmon (landlocked red salmon, Oncorhynchus nerka). J Comparative Physiology A. 174(5):539-49. https://doi.org/10.1007/BF00217373.

Shannon, C.E., 1949. Communication in the presence of noise. P IRE. 37(1):10-21. https://doi.org/10.1109/JRPROC.1949.232969.

Song, Z., Lipinski, D., & Mohseni, K. 2017. Multi-vehicle cooperation and nearly fuel-optimal guidance in strong background flows. Ocean Eng. 141:388-404. https://doi.org/10.1016/j.oceaneng.2017.06.024.

Song, Z., Mazzola, C., Schwartz, E., Chen, R., Finlaw, J., Krieg, M., & Mohseni, K. 2016. A compact autonomous underwater vehicle with cephalopod-inspired propulsion. Mar Technol Soc J. 50(5):88-101. http://dx.doi.org/10.4031/MTSJ.50.5.9.

Xu, Y., & Mohseni, K. 2014. Bioinspired hydrodynamic force feedforward for autonomous underwater vehicle control. IEEE-ASME T Mech. 19(4):1127-37. https://doi.org/10.1109/TMECH.2013.2271037.

Xu, Y., Mohseni, K., 2017. A pressure sensory system inspired by the fish lateral line: Hydrodynamic force estimation and wall detection. IEEE J Ocean Eng. 42(3):532-43. http://dx.doi.org/10.1109/JOE.2016.2613440.